Materials Science & Engineering A 889 (2024) 145816

Contents lists available at ScienceDirect

Materials Science & Engineering A

journal homepage: www.elsevier.com/locate/msea

Texture evolution and hardening behavior of Al/IF composite produced through severe plastic deformation

Ali Shabani [a], Alireza Bagheri [b], Mohammad Reza Toroghinejad [b], Pasquale Cavaliere [a,*]

[a] Department of Innovation Engineering, University of Salento, 73100, Lecce, Italy
[b] Department of Materials Engineering, Isfahan University of Technology, Isfahan, 84156-83111, Iran

ARTICLE INFO

Keywords:
Composite
Accumulative roll bonding
Work hardening
Texture
Microstructure

ABSTRACT

In this research, the microstructure, texture, and work hardening behavior of the Al/IF composite were investigated. The composites were produced through up to 7 cycles of accumulative roll bonding (ARB). The microstructure evolution revealed that the IF layer fractured during the process and distributed within the Al matrix due to its higher hardness and higher work hardening rate, as well as formation of shear bands. The main deformation textures formed in the Al layer were the {001} <110>, {4,4,11} <11,11,8>, and {111} <112> components. In the IF layer, preferred orientations of {001} <110>, {110} <112>, and {111} <110> were observed. The produced composite exhibited typical tensile behavior, with strength increasing and elongation decreasing during the process due to an increment in dislocation density and hardening. Additionally, the results revealed that the hardening capacity of the composite decreased during the process; however, the strain hardening rate increased. A noticeable increase in dislocation density and a decrease in crystallite size were found to be the main governing parameters of these variations. Moreover, the fracture mode of the composite changed from ductile fracture to a more brittle mode as a result of hardening.

1. Introduction

In the last few decades, demand for lightweight metals and alloys in various industries, such as aerospace, automotive, and structural engineering, have remarkably increased with the aim reducing the costs and energy consumption [1,2]. Metal matrix composites (MMCs) based on lightweight metals such as aluminium and titanium have been considered as alternatives to materials currently used in the aforementioned industries due to their specific properties, including low density, high electrical and thermal conductivity, wear resistance, and formability. Recently, numerous research studies have been performed with the aim of improving their production methods and different properties [3–7].

Casting, powder metallurgy, and severe plastic deformation (SPD) are the most commonly used methods for the production of MMCs [8–16]. Accumulative roll bonding (ARB) is among the most used SPD processes, which can be utilized for the production of a vast category of layered and particle-reinforced MMCs [17–21]. The ARB process involves stacking at least two sheets of the same or different materials after suitable annealing and surface treatments, and cold rolling them to achieve a 50% reduction in thickness. The as-rolled sample is then cut into two halves, and the rolling-cutting-rolling process is repeated to reach the desired amount of strain [19,22].

The high level of strain imposed on the composite during the ARB process leads to a remarkable increase in dislocation density and the formation of ultrafine grained microstructures. These two mechanisms (dislocation hardening and grain refinement) are known as the main governing factors of mechanical and microstructural properties, which have been widely reported in different alloying and composite systems [3,19,23,24]. Jiang et al. [25] produced multilayered Ti/Cu composites through the ARB process and reported a significant grain refinement, which was mainly attributed to the formation of shear bands. Wang et al. [24] reported the increment of dislocation density and grain refinement, which were identified as the main strengthening mechanisms, during the ARB of the Al-Li/B_4C composite.

These mechanisms were also reported as the main reasons for the texture variations in the ARB-processed samples [3,13,25–27]. Shabani et al. [13] proposed that the formation of shear bands during cold rolling was the main reason for the development of shear texture. Raei et al. [26] reported that during the ARB process repeating the process of placing the surface of the rolled sheet at the center of the composite and applying pure plane strain compression leads to the rotation of the surface shear texture component toward a single copper rolling

* Corresponding author.
E-mail address: pasquale.cavaliere@unisalento.it (P. Cavaliere).

https://doi.org/10.1016/j.msea.2023.145816
Received 23 August 2023; Received in revised form 22 September 2023; Accepted 17 October 2023
Available online 18 October 2023

component. Subsequently, it rotates back toward a shear texture as it subsequently moves toward the outer surface, leading to an increment in the intensity of the copper component and surface shear component [26].

In addition, it is known that work hardening, due to the increment of dislocation density, strongly affects the final properties of ARB-processed composites; however, the number of published works studying the work hardening behavior of the ARBed composites is negligible compared to the published works in the field of ARB [28,29]. Gashti et al. [30] studied the strain hardening behavior of ultrafine-grain ARBed AA1050 alloy and reported that the strain hardening rate of ARBed samples increased with an increase in the number of ARB cycles and was mainly governed by the two factors: dislocation density and grain size. Moradgholi et al. [29] claimed that the work hardening coefficient of Ti/TiO_2 composite produced through the ARB process increased with the addition of TiO_2 particles and reported that the dislocation tangles around TiO_2 nanoparticles were the main cause of the increase in the work hardening coefficient.

The main objectives of this research were to investigate the texture evolution and work hardening behavior of Al/IF during the ARB process. To achieve this, the Al/IF composite was produced through a maximum of 7 ARB cycles. Then, using an optical microscope (OM), scanning electron microscope (SEM) equipped with an electron backscattered diffraction (EBSD) detector, X-ray diffraction (XRD), and tensile test, the behavior of the composite was studied during the process.

2. Materials and method

The raw materials included commercially pure Al and IF steel strips with the specifications given in Table 1. Strips with dimensions of 50 × 100 × 1 mm and 50 × 100 × 0.7 mm were cut along the primary rolling direction (RD) from the Al and IF sheets, respectively, and then, were, respectively, annealed at 350 and 650 °C for 60 min. Before rolling, the strips were washed in an acetone bath and wire brushed along the RD for 2 min. In the first ARB cycle, the IF strip was laid between the two annealed Al strips and fastened at both ends using steel wire, and then, roll-bonded to 66% reduction to attain a strip with 1 mm thickness. The produced sandwich was then ARBed for up to 7 cycles through the typical ARB process. A detailed explanation of the process can be found elsewhere [20,31].

The crystal structure of the composites after each cycle was investigated using an X-ray diffractometer (Philips, Amsterdam, Netherlands) with Cu Kα (λ = 0.15406 nm) diffraction and the step size of 0.05°. In addition, crystallite size and micro-strain of different samples were calculated by analyzing the XRD patterns using Rietveld software, specifically Materials Analysis Using Diffraction (MAUD) [32,33]. MAUD has been widely used to characterize microstructural parameters including lattice parameters, phase percentage, crystallite sizes, and residual micro-strains based on XRD results [34–36]. In addition, tensile test samples were machined from composites after each cycle through electrical discharge machining (EDM) according to the ASTM E8M standard. The gauge width and length were 6 and 25 mm, respectively. Tensile tests were conducted at room temperature using a tensile testing machine (H25KS; Hounsfield Ltd., Surrey, UK).

3. Results

3.1. Microstructural and structural analysis

OM micrographs of the composite at different ARB cycles are presented in Fig. 1. As can be seen, in the primary sandwich structure, the layers remained stable, and no fracture occurred within the composite layers. However, with the continuation of the ARB process, fracture and separation initiated in the IF layer as shown in Fig. 1b. With the repetition of the ARB cycle and increase in the strain amount in the composite sample, the thickness of the IF layers decreased, and the fracture and separation of the IF fragments took place at an increasing rate. Eventually, an Al matrix composite with an almost uniform distribution of IF fragments was achieved after 7 cycles of the ARB process. It is noteworthy that shear bands formation was observed in the composites with an increase in the strain amount as marked in Fig. 1d.

XRD test was performed on the composites after different ARB cycles and the results are presented in Fig. 2. As can be seen, all the peaks are related to the Al and IF in the primary sandwich, and they remained unchanged as ARB proceeded up to 7 cycles; no phase transformation took place during the process. In addition, the intensity of the peaks varied during the process which can be attributed to the texture formation and is further studied in the following sections.

Using MAUD software and the XRD patterns of the composite, different structural parameters such as crystallite size and micro-strain of the composites were measured after each cycle. Fig. 2a illustrates that crystallite size of the Al and IF layers after the first cycle were 270 and 150 nm, respectively, and decreased almost 15% in both layers with an increase in the number of ARB cycles to 3. The crystallite size then declined almost linearly in both layers with the repetition of the ARB process and reached 125 and 90 nm in Al and IF layers, respectively. Variation in micro-strain of the Al and IF layers as a function of ARB cycles is presented in Fig. 2b. This figure demonstrates that the amount of micro-strain in the IF layer was higher than that in the Al layer after the primary cycle of ARB, and it remained higher as the process continued. In addition, the amount of micro-strain increased in both layers with the continuation of the ARB process; however, the rate of increase in micro-strain in the Al layer dropped after the fifth cycle.

Using the following equation, the dislocation density of the Al and IF layers was measured and is shown in Fig. 4. This figure depicts that the dislocation density was higher in the IF layer after the first cycle (0.09 and 0.34 × 10^{14} in Al and IF layers, respectively) and increased almost linearly in both layers with an increase in the number of ARB cycles up to 7 cycles. In addition, it can be seen that the dislocation density in Al and IF increased, respectively, by 11 and 7 times after 7 cycles; however, the amount of new dislocation formed during the process in IF was higher than that in Al by almost two times (0.96 and 2.11 ×10^{14} dislocations in Al and IF layers, respectively).

$$\rho = \frac{2\sqrt{3.\varepsilon}}{Db} \quad \text{(eq.1)}$$

3.2. Texture evolution

Figs. 5 and 6 illustrate the φ_2 = 0°, 45°, and 65° sections of the orientation diffraction functions (ODFs) of the Al and IF layers, respectively, after different ARB cycles. The main texture components studied

Table 1
Specifications of the used materials.

Material	Al	Fe	Si	Mn	Ni	C	Ti	Cu
Al	99.71	0.16	0.07	0.007	0.001	-	0.01	-
IF	-	99.94	0.01	0.14	0.02	0.002	0.05	0.01

The microstructure of the composite was examined on the rolling direction-normal direction (RD-ND) plane using an OM. In addition, texture and fracture surfaces after tensile test were examined via an SEM-EBSD (FEI, XLF30; Philips, Amsterdam, Netherlands).

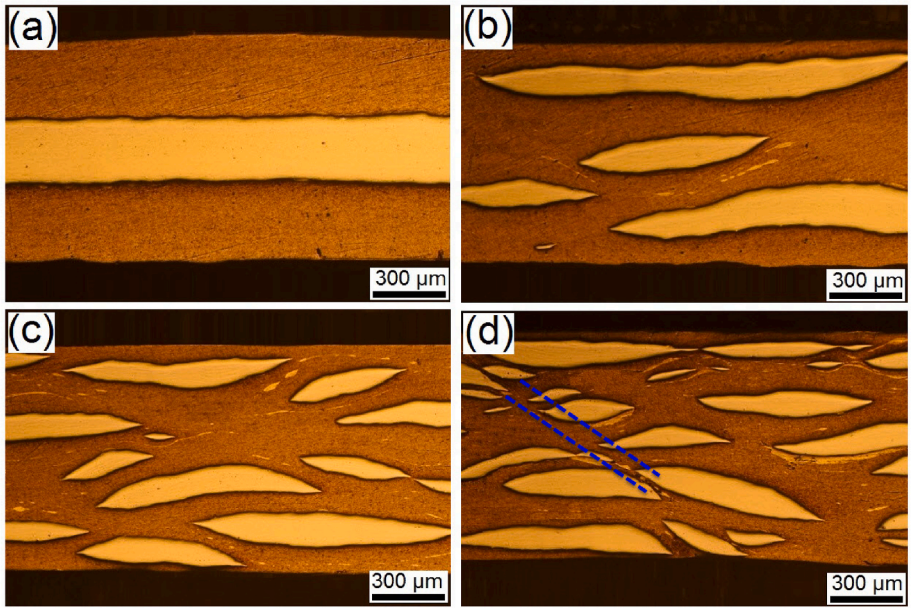

Fig. 1. OM microstructure of Al-IF samples after a) 1 cycle, b) 3 cycles, c) 5 cycles, and d) 7 cycles of ARB.

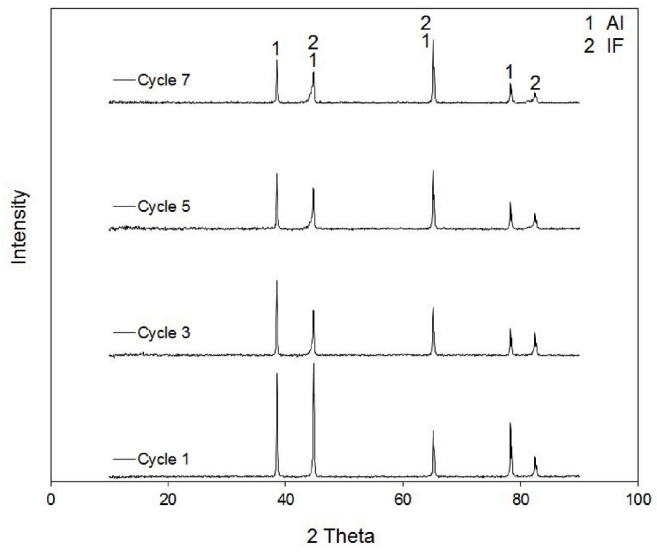

Fig. 2. XRD patterns of the composite after different ARB cycles.

here are presented in Table 2. As can be seen in Fig. 5a, {110} <001> and {110} <111> were the main texture components in Al after the first ARB cycle. With the continuation of the ARB process to the third cycle,

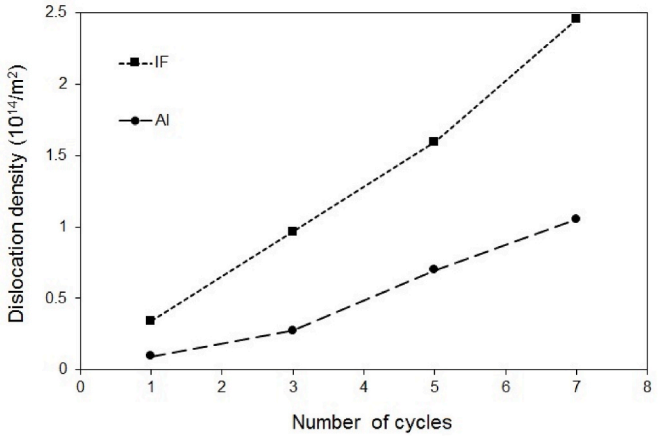

Fig. 4. Variation in dislocation density of the Al and IF layers as a function of ARB cycle.

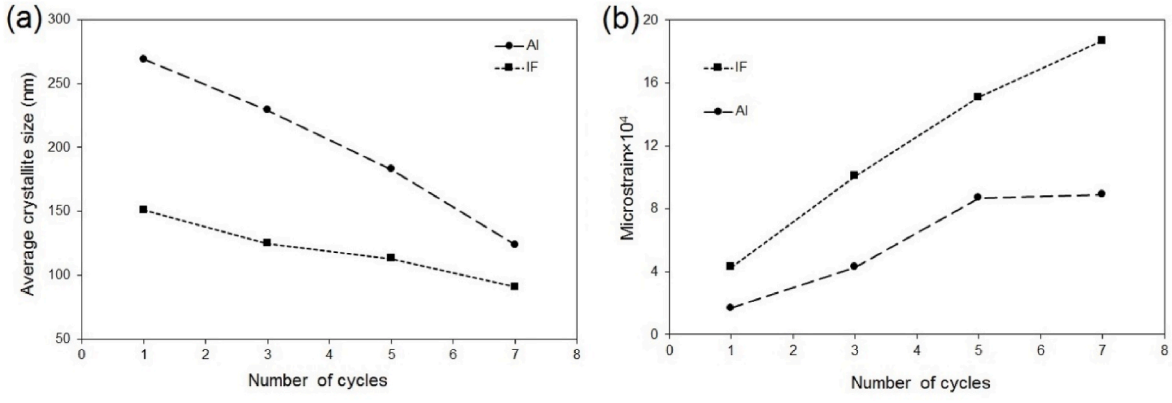

Fig. 3. Variation in a) average crystallite size and b) micro-strain of the Al and IF layers during the ARB process.

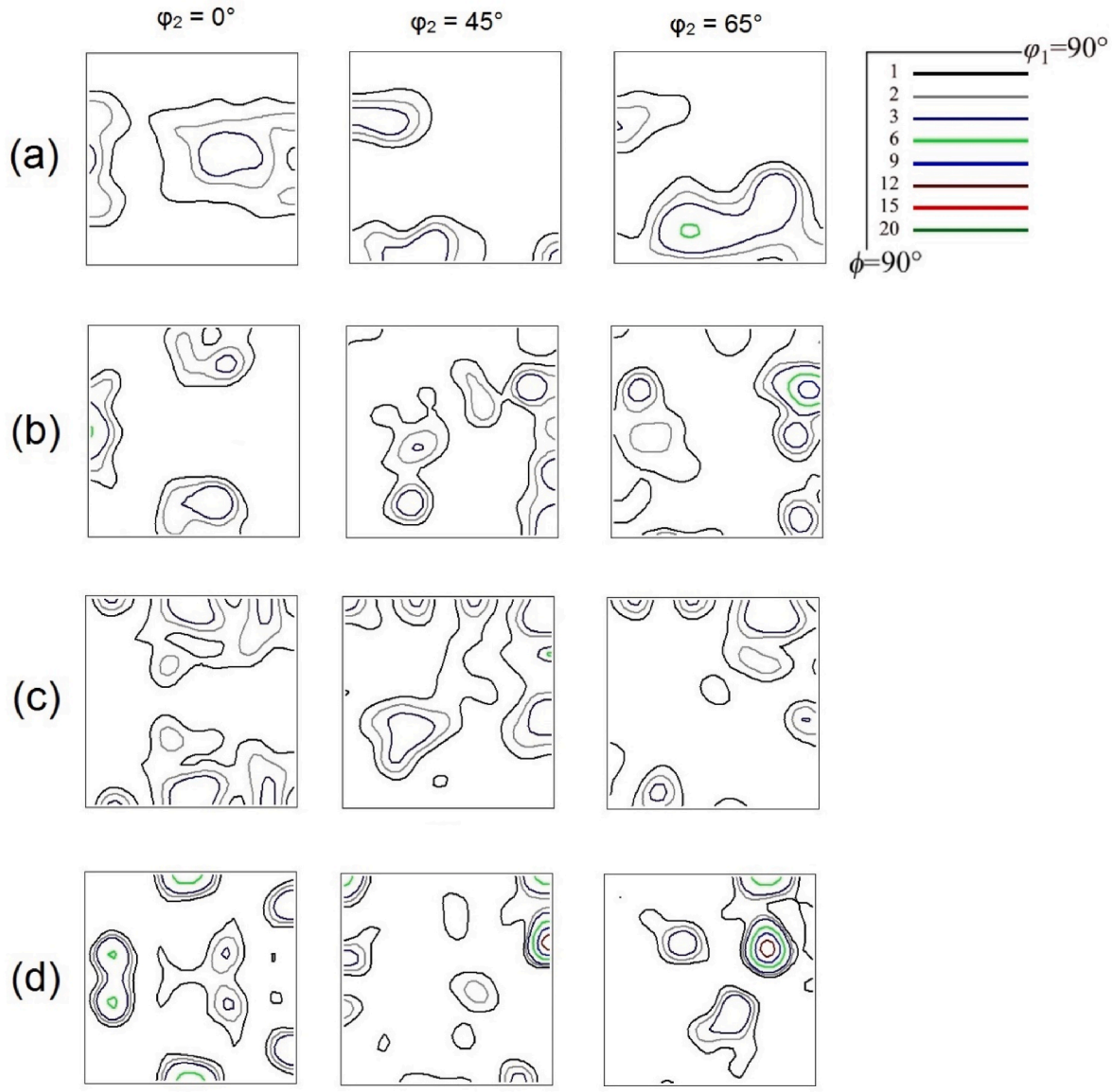

Fig. 5. The $\varphi_2 = 0°$, 45°, and 65° sections of the ODFs of the Al layer after cycle (a) 1, (b) 3, (c) 5, and (d) 7.

{110} <001> still remained as a strong texture component; however, a weak {4,4,11} <11,11,8> component formed in the Al layer during this cycle. After 5 cycles of ARB, the primary texture components were entirely eliminated, and the {001} <110> and {4,4,11} <11,11,8> components were the major texture in Al at this stage. As revealed in Fig. 5d, the continuation of the ARB process to the seventh cycle has not changed the preferred orientations, and {001} <110> and {4,4,11} <11,11,8> remained with higher intensity as the main texture components in the Al layer.

Fig. 6a demonstrates that, in the IF layer, {110} <001> and {110} <111> were the main texture components; however, both were eliminated after the third cycle, in which {110} <110> and {111} <110> became the major texture components in the presence of the weak intensity components of {110} <112>, {112} <110>, and {001} <110>. After the fifth cycle of the process, the main texture in the IF layer consisted of {001} <110>, {111} <110>, and {112} <110>. Increasing the number of ARB cycles to 7 did not lead to a significant change in the texture of the IF layer; however, the intensity of the components increased, as revealed in Fig. 6d.

In order to gain a better understanding of the variations in texture, the maximum intensities of the texture components were depicted as a function of ARB cycle, which is presented in Fig. 7. It can be seen that, in the Al layer, the intensity of the {110} <001> and {110} <111> components declined with the continuation of the ARB process; however, the intensities of the {111} <112>, {001} <110>, and {4,4,11} <11,11,8> components increased with an increase in ARB cycles, which was significant in the {001} <110> and {4,4,11} <11,11,8> components. Additionally, Fig. 7b illustrates that, during the ARB process, the intensity of the {110} <001>, {110} <110>, and {110} <111> components decreased, and the ARB process led to the intensifying of the {001} <110>, {110} <112>, and {111} <110> texture components.

3.3. Mechanical properties

Fig. 8 illustrates the tensile behavior of the composites at different ARB cycles in comparison to the annealed Al. It is evident that the formability of the composites decreased significantly compared to the annealed Al; however, the strength of the composites was noticeably higher. Furthermore, it can be seen that the strength of the composite increased with the continuation of the ARB process; however, its

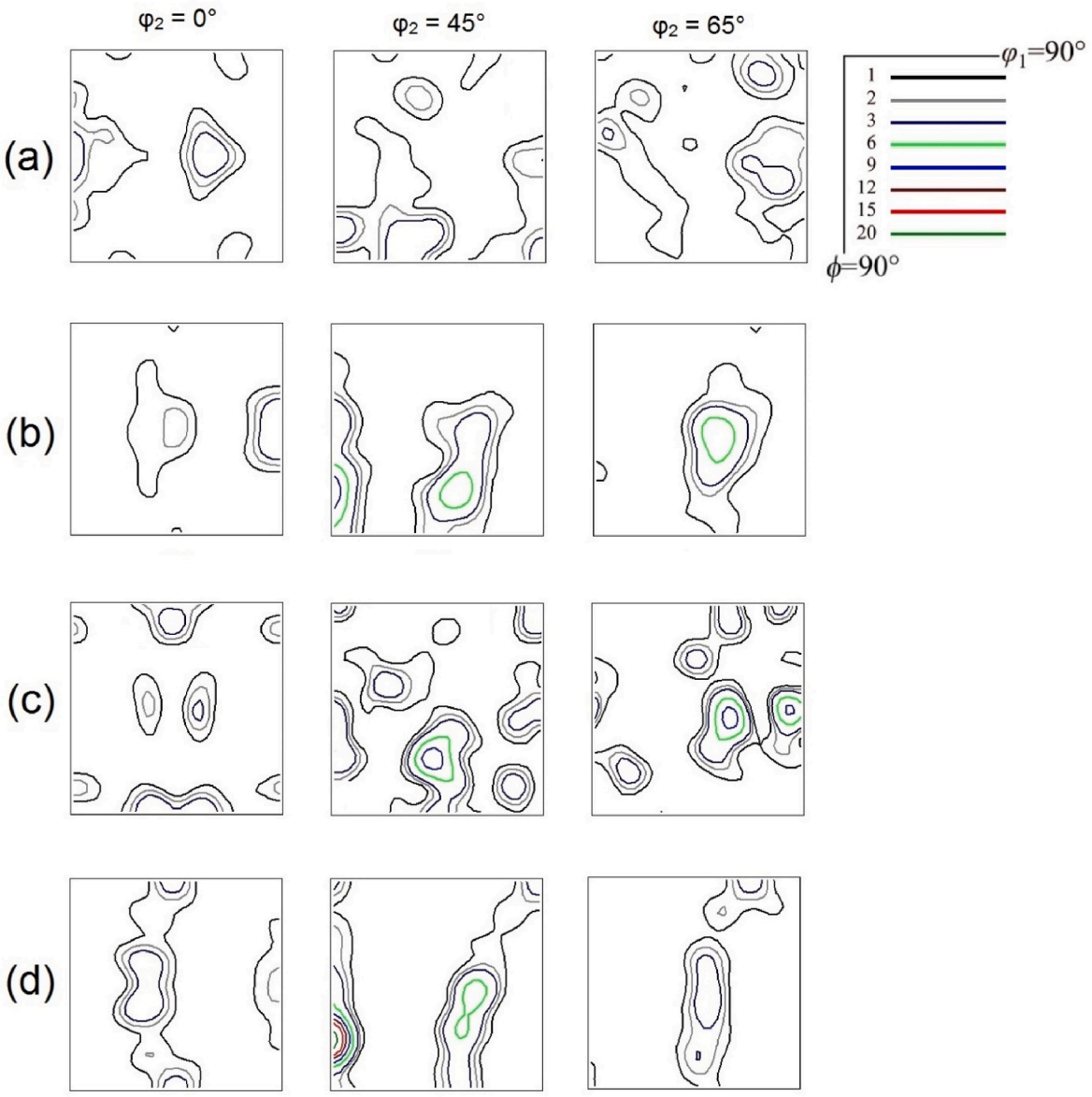

Fig. 6. The φ2 = 0°, 45°, and 65° sections of the ODFs of the IF layer after cycle (a) 1, (b) 3, (c) 5, and (d) 7.

Table 2
The main texture components studied in this research.

Miller indices	φ_1	Φ	φ_2
{110}<001>	0	45	0
{110}<111>	55	45	0
{110}<110>	90	45	0
{110}<112>	35	45	0
{001}<110>	0	0	45
{111}<110>	0	45	55
{123}<634>	59	37	63
{111}<112>	30	45	55
{4,4,11}<11,11,8>	90	27	45

formability decreased. Fig. 9 illustrates the variations in strength and elongation of the composite as functions of the ARB cycle. The yield strength (YS) of the annealed Al was about 60 MPa, which sharply increased to almost 195 MPa, indicating more than 220% increment, and then gradually increased with the continuation of the ARB process. As shown in Fig. 9a, an almost 7, 10, and 9% increment in YS took place after the third, fifth, and seventh ARB cycle, respectively. Fig. 9b indicates that variation in the ultimate tensile strength (UTS) was almost the same as YS; a sharp increment in UTS (almost 140%) occurred after the first cycle, and then it increased gradually to its maximum amount after the seventh cycle (about 290 MPa). Variation in elongation with an increase in the number of ARB cycles is presented in Fig. 9c, and it shows that the elongation of the composite varied, unlike the strength variation. In the annealed Al, almost 28% elongation was observed, which reached 9% after the first cycle of ARB, and then declined at the rate of 30, 16, and 16% after cycles 3, 5, and 7, respectively, and almost 4.2% elongation was observed in the final composite.

Using simple Hollomon's equation [37,38] (eq. (2)), the strain hardening exponent (n) of the composites could be measured as follows:

$$\sigma = K\varepsilon^n \quad \text{(eq.2)}$$

$$n = d(In\sigma)/d(In\varepsilon) \quad \text{(eq.3)}$$

Therefore, n can be measured by sketching the lnσ-lnε curve, in which n is the slope of the curves. The lnσ-lnε curves for the composites after different ARB cycles are presented in Fig. 10 with the measured slopes. As can be seen, the n parameter decreased with the increase in

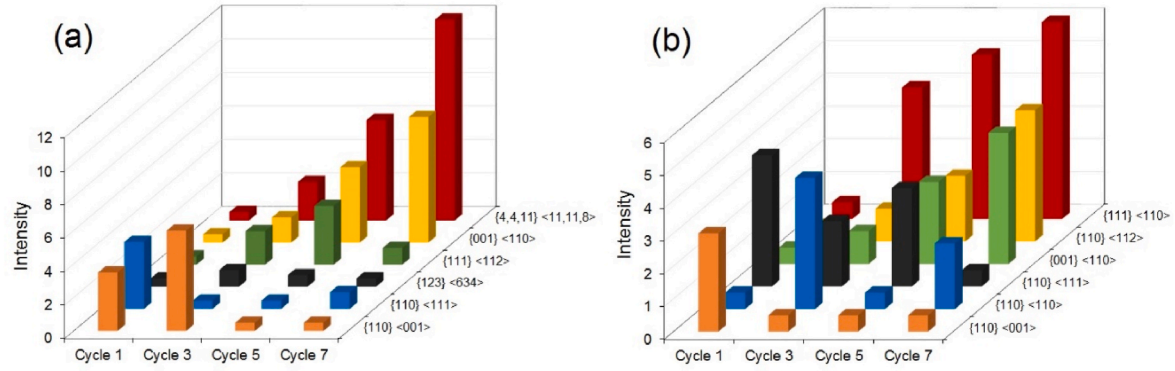

Fig. 7. Variations in texture intensity as a function of the ARB cycle in a) Al layer and b) IF layer.

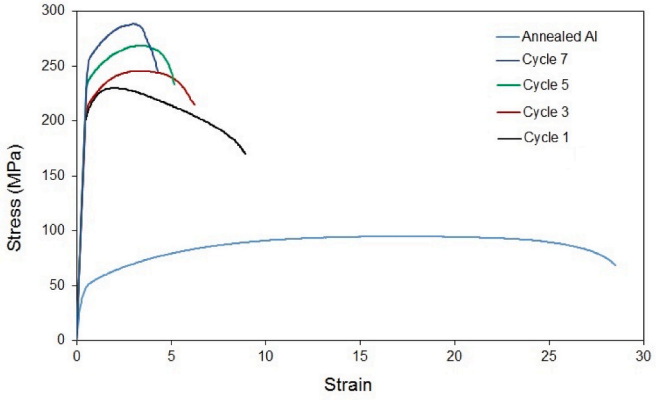

Fig. 8. Stress-strain curves of the tensile behavior of the composites after different cycles of ARB in comparison to the annealed Al.

the number of ARB cycles. The n parameter was almost 0.089 after the first cycle, which declined gradually with the continuation of the ARB process and reached almost 0.77 after 7 cycles of ARB.

In addition, using the following equation [39,40], the hardening capacity (H_C) of the composites was measured and the results are presented in Fig. 11.

$$H_c = \frac{\sigma_{UTS} - \sigma_y}{\sigma_y} = \frac{\sigma_{UTS}}{\sigma_y} - 1 \quad \text{(eq.4)}$$

In the above equation, σ_{UTS} is the UTS, and σ_y is the YS. Fig. 11 illustrates that the H_C of the composite decreased with an increase in the number of ARB cycles. The H_C of the composite after the first cycle was almost 0.167, which decreased to 0.161 after the second cycle. The decline in the H_C took place at a higher rate, and it reached 0.140 and 0.125 after the fifth and seventh cycles, respectively.

Furthermore, Fig. 12 illustrates the strain hardening rate of the primary raw materials and the composites after different ARB cycles. As can be seen in this figure, the work hardening rate in the IF layer was higher than that in the Al layer. In addition, in contrast to the n and H_C, the strain hardening rate increased with the continuation of the ARB process. It is evident that the trend of variation in strain hardening rate was almost the same in all the composites and had two different stages. In the first stage, the strain hardening rate was noticeably high at the beginning of the tension test, and then it sharply decreased with an increase in strain amount at the initial stage of deformation. In the second

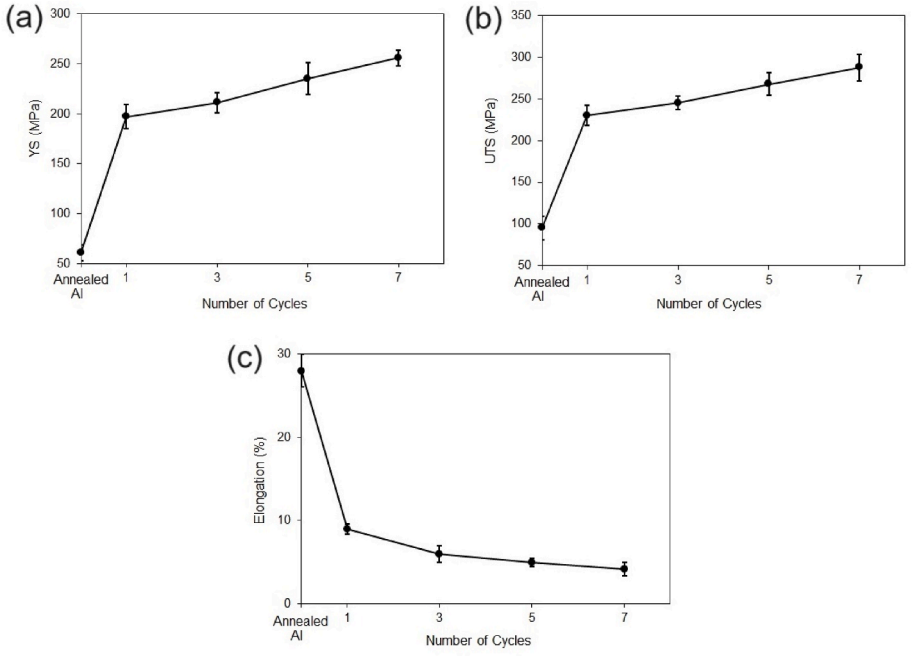

Fig. 9. Variations in the a) YS, b) UTS, and c) elongation of the composite as a function of the ARB cycle.

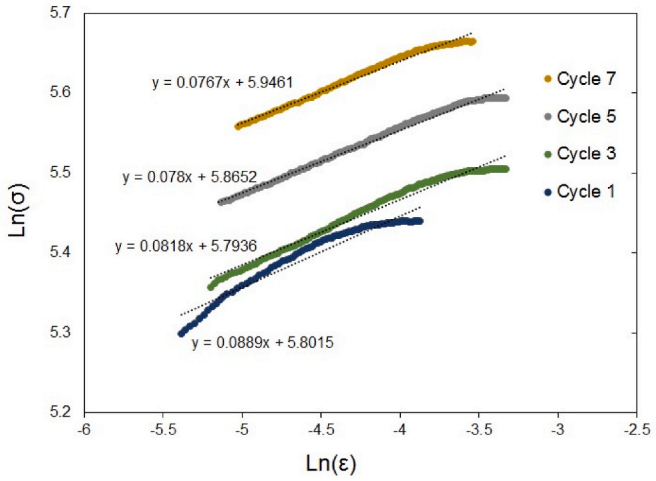

Fig. 10. lnσ-lnε curves for the Al/IF composites after different cycles of ARB.

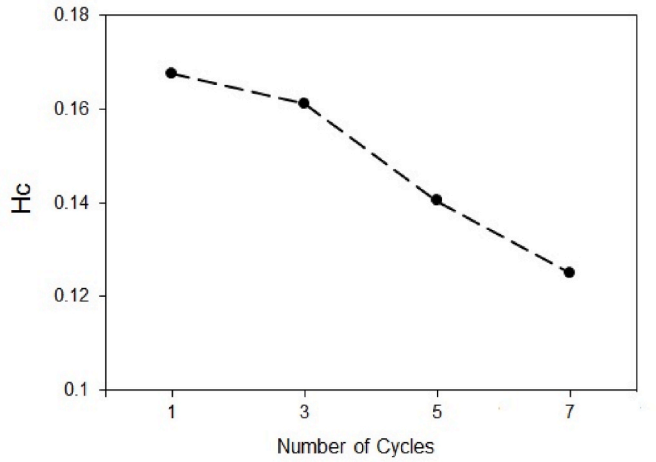

Fig. 11. Variation in H_C of the composite with increase in the number of cycles of the ARB process.

stage, the strain hardening rate declined at a slower rate until the cessation of uniform deformation, at which point the strain hardening rate reached zero.

Fracture surfaces of the composites after tensile tests were examined using SEM to determine the fracture mechanisms of the composites in different cycles of the ARB process. Fig. 13a shows that a typical ductile fracture occurred in both layers after the first cycle, with the fracture surface fully covered with equiaxed dimples. Additionally, the occurrence of lamination during tension is evident in this figure, revealing the low quality of bonding in this stage. As illustrated in Fig. 13b, the fracture mode changed after the third cycle, with some parts of the fracture surface appearing smooth, indicative of brittle fracture. However, dimple formation and ductile fracture still seemed to be the main fracture mode in this sample. The fracture mode further changed after the fifth cycle of ARB, with a significant portion of the fracture surface exhibiting smooth features (brittle fracture), and the size and number of the dimples decreased noticeably. In addition, the orientation of the dimples also changed, with shear dimples (shear-ductile fracture) forming on the fracture surface of this sample (see Fig. 13c). Fig. 13d demonstrates the fracture surface of the composite after 7 cycles, and it can be observed that the fracture surface differed completely from that of the primary composite. The majority of the fracture surface revealed a brittle fracture mode, with only a few small shear dimples present.

4. Discussion

In the ARB technique, the primary dissimilar multi-layered sandwich can change to a metal matrix composite with an almost uniform distribution of the fragments of one of the layers. Different metals have different mechanical properties and react differently to the deformation processes. During the ARB process, roller pressure leads to elongation of the layers along the RD and a decrease in their thickness; moreover, different flow properties of the layers could lead to the occurrence of plastic instabilities, and finally, the fracture of the layers [18,20,41]. This phenomenon has been reported in different dissimilar multi-layered composites. For instance, Jiang et al. [19] reported that in Ti/Nb composite, Nb layers begin to neck and even rupture with an increase in the number of ARB cycles, which was attributed to the higher hardness of the Nb layer and curvature of interfaces. Jafarian et al. [18] claimed that non-uniform plastic strain distribution due to the different mechanical properties and strain hardening parameters is the governing parameter in the fracture of layers during the ARB process. In addition, they reported that the Ni layer with the highest strain hardening coefficient was the first layer to fracture [18]. Generally, during the ARB process, the thickness of the layer decreases by 50% after each cycle [22,42] and fracture takes place in the layer with the highest resistance to decrease in the thickness. In fact, the layer with a higher work hardening rate hardens faster and resists the applied pressure of the roller, and therefore, fracture occurs as a result of work hardening and an increase in the applied stress to the ultimate strength of the layer. Fig. 12a illustrates that the work hardening rate in the IF layer was higher than that in the Al layer, which is the main reason for the fracture of this layer during the ARB process, as shown in Fig. 1.

In addition, the repetition of the rolling process leads to the formation of a high amount of dislocation in the sample (Fig. 4) and an extremely high level of work hardening, which results in more brittle

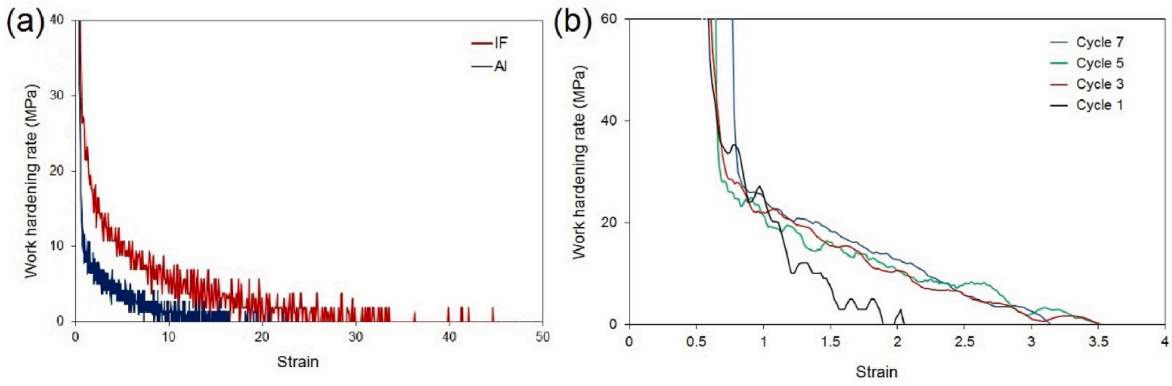

Fig. 12. Work hardening behavior of the a) primary raw materials and b) composites after different ARB cycles.

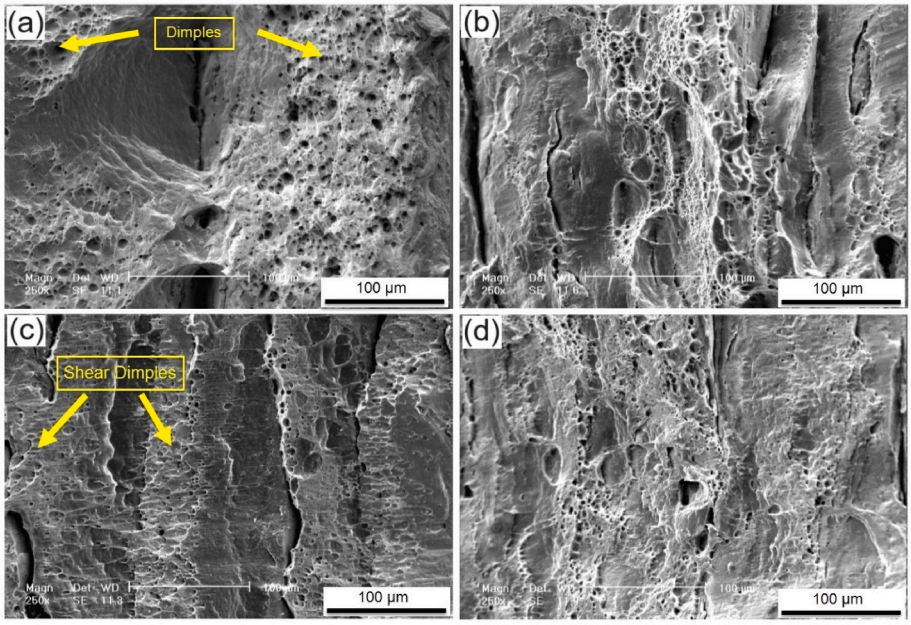

Fig. 13. SEM images of the fracture surfaces of the Al/IF composite after the a) first cycle, b) second cycle, c) fifth cycle, and d) seventh cycle of ARB.

behavior. Consequently, this makes the layer more susceptible to fracture in the final cycles of the process. Furthermore, the formation of shear bands during the ARB process has been widely reported [20,43,44]. Shear bands generally form during rolling at almost 35-45° to the RD and occur independently of the grain structure of the sample [45]. The formation of shear bands was revealed in Fig. 1 and it can be seen that their formation is an influential factor in the fracture of layers during the process. A high-magnification micrograph of the sample after 7 cycles of ARB is illustrated in Fig. 14a, which clearly shows the formation of a shear band that leads to the fracture and separation of the IF layer. Shear bands initiate on the surface of the specimen in contact with the rolls and propagate towards the opposite surface. They not only generate strain fields along the shear band direction but also create strong strain fields that extend well into the material surrounding the band [19,43,45], which might increase to amounts higher than the strength of the materials. In addition, Scudino [46] reported that the formation of shear bands induces atomic displacements at opposite directions on the two sides of the band, and therefore, the neighboring unsheared material induces tensile and compressive strains in the direction parallel to the band. Fig. 14a illustrates that the formation of shear bands and induction of strain in opposite directions led to the fracture of the IF layer, and this mechanism is schematically presented in Fig. 14b.

As revealed in Figs. 5 to 7, the texture of both Al and IF layers varied as a function of the number of ARB cycles. In the Al layer, the intensity of the {110} <001> component decreased, and the {001} <110>, {4,4,11} <11,11,8>, and {111} <112> components intensified. The formation of these components during ARB of Al has been reported in previous research studies [13,26,27]. The microstructure of the ARBed composites (Fig. 1) showed the formation of shear bands, which is the main reason for the formation of shear texture components in FCC metals [13,47]. Moreover, the cyclic movement of the shear components formed on the surface to the center of the composite during the process and induction of extra strain during the rolling cycles are reported to be a result of shear texture formation [26].

In addition, it was seen that the intensity of {110} <001> and {110} <110> in the IF layer decreased, while {001} <110>, {110} <112>, and {111} <110> intensified during the ARB process. These components are known as the rolling texture and shear texture, and their formation during rolling of BCC metals has been reported [19,48]. Jamaati et al. [48] reported that, during the ARB process, the slip planes might rotate toward the direction perpendicular to the roller force, and the rotation will not occur completely due to the resistance to the deformation as a result of crystal defects, which resulted in the rotation of other crystal planes parallel to the rolling plane and the formation of rolling texture components. The increase in the intensity of the brass component was also attributed to the formation of deformation twins and the enhancement of the spacing between dislocation cell boundaries

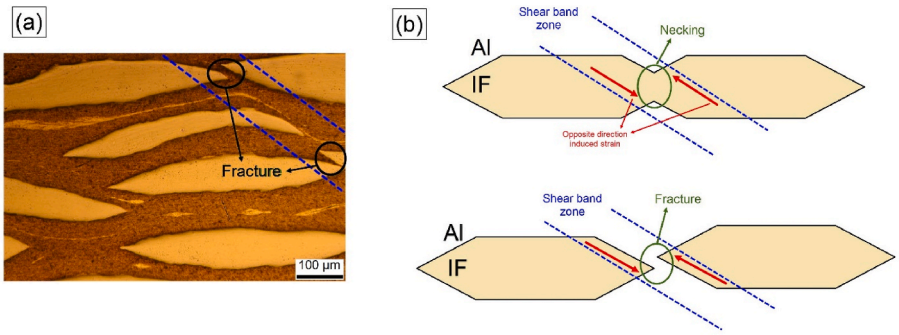

Fig. 14. a) A high magnitude micrograph of the composite after 7 cycles of ARB and b) schematic illustration of the fracture mechanism of the IF layer as result of shear band formation.

due to severe plastic deformation and hardening [48].

Hitherto, it has been demonstrated in different ARB-processed metals and alloys that their strength and elongation increase during the process [18,20,28]. Work hardening due to the increase in dislocation density and grain refinement has been reported as the main reason for this increase in strength and elongation [20,28,30]. Figs. 3 and 4 illustrate that with an increase in the strain amount during the process, the crystallite size decreased sharply, while the density of dislocation in both Al and IF layers increased significantly, which were the governing parameters of the mechanical properties as explained above. In addition, the ARB technique has been widely used for the production of metal matrix composites, and variations in different characteristics of the composites have been reported as the effective parameter on mechanical properties [41,42,49,50]. For instance, Rahmatabadi et al. [41] claimed that, the volume, size, and distribution of the reinforcement particles in the composite were effective on mechanical properties. Habba et al. [51] asserted that during the ARB process of Al-Ni/SiC composites, the distribution of the SiC particles becomes more uniform which positively affects the mechanical properties. However, they revealed that a high amount of reinforcement can lead to the separation of layers and a drop in strength.

Generally, the size of the second-phase particles decreased during the process. It has been revealed that the ARB process carried out on metals causes plastic deformation in the sheets, and the reinforcement particles break. Therefore, repeating the ARB process leads to a finer and more uniform distribution of the reinforcement, and consequently, the distances between these particles remarkably decrease. During deformation, reinforcement particles operate as an imminent displacement movement, and more dislocation also generates at the interface of the particles and matrix. These phenomena led to an increase in the resistance of the microstructure to the passing of dislocations, which led to higher UTS [23,49,52].

The results presented in Figs. 10 to 12 reveal that the values of n and H_C decreased with the continuation of the ARB process; however, the rate of the strain hardening increased. It is known that the density of dislocations and grain size are the two main governing parameters of hardening capacity during the ARB process [39,40]. With the continuation of the ARB process, dislocation density increased at a noticeable rate (see Fig. 4); therefore, the interaction between dislocations increased, leading to higher resistance to deformation, and consequently, lower hardening capacity. Additionally, the grain size of the ARBed samples decreased sharply (see Fig. 3) with an increase in the ARB cycles. Furthermore, the formation of nano-size grains during the process has been widely reported [48,53]. Therefore, the possible slip distance of the dislocation to reach a grain boundary decreases due to the decrease in grain size, which leads to a lower possibility of further deformation and hardening. Fattah-alhosseini et al. [28] reported almost the same results on the work hardening behavior of copper subjected to the ARB process. They showed that n value decreased with the continuation of ARB process as a result of grain refinement [28]. The increment of the strain hardening rate with an increase in the number of ARB cycles is also attributed to the increase in dislocation density and grain refinement, which led to a higher rate of dislocation collision and lower slipping distance of dislocations, and consequently, a higher work hardening rate. In a recent research, Gashti et al. [30] reported the same hardening behavior in ARBed Al in which the n value decreased and strain hardening increased with the continuation of the ARB process as a result of dislocation density enhancement and grain refinement.

In addition to dislocation interactions and the shortened slipping distance resulting from grain refinement, other critical parameters contribute to the hardening behavior of the composite. One of these key factors is grain boundary strengthening, which exerts a substantial influence. During the process of high-strain plastic deformation, an essential role is played by the formation of new grain boundaries characterized by high misorientation angles, as well as the development of dislocation cells (DCs) with relatively low misorientations. These structural features significantly enhance the overall hardening of the composite [45,47].

As the deformation level increases, significant changes occur. On one hand, the layers undergo substantial stretching along the rolling direction, potentially facilitating the formation of new grain boundaries and enhancing the overall ratio of boundaries within the composite structure. Simultaneously, dislocation density noticeably increases (see Fig. 4), subsequently leading to the rearrangement of dislocations within the DC structure. These dynamic phenomena directly and substantially affect the hardening behavior exhibited by the composite. Consequently, with the progressive increase in the grain boundary portion within the structure, grain boundary strengthening occurs. This, in turn, results in an accelerated hardening rate. However, concurrently, the overall hardening capacity decreases [36,47,51].

Moreover, the hardening of the composite intensifies significantly due to the presence of reinforcements with hardness differing from the matrix. During the process of rolling, the Al and IF layers exhibit distinct deformation characteristics, each responding uniquely to the external forces applied. In order to maintain coherence between the reinforcement particles and the matrix material, geometrically necessary dislocations (GNDs) emerge at the interfaces of these particles [45,47]. These dislocations play a crucial role in enhancing the overall hardening rate of the composite. This phenomenon intensifies with improvement of the ARB process, leading to a remarkable boost in the composite's mechanical properties. As seen in Fig. 1, the fracture of the IF layer during the ARB process results in the dispersion of IF particles throughout the composite structure. This dispersion of particles further accelerates the formation of GNDs, particularly at higher ARB cycles.

Additionally, the reinforcements serve as effective barriers to the movement of dislocations within the composite [31,51]. This function plays a significant role in the hardening behavior, acting as a resistance force against dislocation motion. As explained earlier, the uniformity and number of these reinforcement particles increase with the improvement of the ARB process. This enhancement in distribution and the higher number of reinforcement particles lead to more frequent interactions between dislocations and the particle interfaces. As a consequence, this heightened level of interaction contributes to a substantially increased hardening rate.

Hardening during the ARB process noticeably affects the fracture behavior, which has been widely reported in the processing of different alloys and composites [13,20,29,31]. In the primary stages of the process, a ductile fracture takes place with a high amount of plastic deformation, leading to the formation of a rough fracture surface with deep equiaxed dimples. These dimples form due to the creation of microvoids and the final rupture after their coalescence [31,54]. With an increase in the number of ARB cycles, the density of dislocations increases (Fig. 4) due to the significant amount of plastic deformation. Consequently, the plasticity of the sample decreases, which changes the fracture mode to a more brittle fracture (Fig. 13). Additionally, it was observed that the separation of the layers occurred more evidently in the first cycle of the process (see Fig. 13a), which is a result of weak bonding quality between the layers and also different deformation behaviors of the layers [20,31], leading to separation during tensile deformation. However, delamination at higher levels of strain was observed in the composite, which is due to the stress concentration at the interface of the particles. During deformation, too many GNDs form at the interface, and sliding can also lead to the accumulation of dislocations at the interface, resulting in the formation of stress concentration regions that fracture more easily during tensile deformation, leading to the separation of particles from the matrix.

5. Conclusion

In this research, Al/IF composite was produced through ARB technique with up to 7 cycles. Variations in its microstructure, texture, tensile properties, and work hardening behavior were investigated using

SEM-EBSD, XRD, and tensile test. The following conclusions can be drawn:

1. ARB process led to the fracture of the IF layer which was attributed to its higher hardness and work hardening rate compared to Al. Shear bands played a crucial role in the increased fracture rate during the later stages of ARB.
2. The continuation of the ARB process resulted in the formation of shear texture in the composite, involving specific texture components in both the Al and IF layers. Texture evolution was primarily driven by the formation of shear bands and slip plane rotation.
3. The composite's strength increased with ARB cycles, reaching a UTS of 290 MPa, although the elongation reduced. These changes were linked to increased dislocation density, smaller crystallite size, and the presence of IF fragments as reinforcement.
4. The ability of the composite to harden (n and H_C values) decreased with the continuation of the process; however, the work hardening rate increased. This behavior was governed by increased dislocation density, enhanced dislocation interactions, and grain refinement reducing dislocation slip distances.

CRediT authorship contribution statement

Ali Shabani: Formal analysis, Investigation. **Alireza Bagheri:** Formal analysis, Investigation. **Mohammad Reza Toroghinejad:** Conceptualization, Supervision. **Pasquale Cavaliere:** Conceptualization, Supervision, Data curation, Writing – original draft, Writing – review & editing.

Declaration of competing interest

The authors declare that they have no known competing financial interests or personal relationships that could have appeared to influence the work reported in this paper.

Data availability

Data will be made available on request.

References

[1] S. Prasad, R. Asthana, Aluminum metal-matrix composites for automotive applications: tribological considerations, Tribol. Lett. 17 (3) (2004) 445–453.
[2] P. Rohatgi, Cast aluminum-matrix composites for automotive applications, Jom 43 (4) (1991) 10–15.
[3] N. Hosseiny, A. Shabani, M.R. Toroghinejad, Effect of bimodal microstructure on texture evolution and mechanical properties of 1050 Al alloy processed through severe plastic deformation and subsequent annealing, Mater. Sci. Eng., A (2021), 141580.
[4] A. Shabani, M.R. Toroghinejad, A. Shafyei, Effect of post-rolling annealing treatment and thickness of nickel coating on the bond strength of Al–Cu strips in cold roll bonding process, Mater. Des. 40 (2012) 212–220.
[5] L. Huang, Q. An, L. Geng, S. Wang, S. Jiang, X. Cui, R. Zhang, F. Sun, Y. Jiao, X. Chen, Multiscale architecture and superior high-temperature performance of discontinuously reinforced titanium matrix composites, Adv. Mater. 33 (6) (2021), 2000688.
[6] I. Najjar, A. Sadoun, M. Alam, A. Fathy, Prediction of wear rates of Al-TiO2 nanocomposites using artificial neural network modified with particle swarm optimization algorithm, Mater. Today Commun. 35 (2023), 105743.
[7] I. Najjar, A. Sadoun, A. Ibrahim, H. Ahmadian, A. Fathy, A modified artificial neural network to predict the tribological properties of Al-SiC nanocomposites fabricated by accumulative roll bonding process, J. Compos. Mater. (2023), 00219983231186205.
[8] P. Cavaliere, F. Jahantigh, A. Shabani, B. Sadeghi, Influence of SiO2 nanoparticles on the microstructure and mechanical properties of Al matrix nanocomposites fabricated by spark plasma sintering, Compos. B Eng. 146 (2018) 60–68.
[9] A. Shabani, M.R. Toroghinejad, A. Bagheri, Effects of intermediate Ni layer on mechanical properties of Al–Cu layered composites fabricated through cold roll bonding, Int. J. Miner. Metall. Mater. 25 (5) (2018) 573–583.
[10] P. Cavaliere, B. Sadeghi, A. Shabani, Carbon nanotube reinforced aluminum matrix composites produced by spark plasma sintering, J. Mater. Sci. 52 (14) (2017) 8618–8629.
[11] A. Bagheri, A. Shabani, M.R. Toroghinejad, A. Taherizadeh, Post-rolling annealing of a multilayered Brass/IFS/Brass composite: an evaluation of anisotropy, formability, and mechanical properties, J. Mater. Res. Technol. 19 (2022) 732–746.
[12] Z. Chang, Y. Wu, T. Iizuka, L. Peng, W. Ding, High-strength and high-modulus Al18B4O33W/GWZ1031K magnesium matrix composite prepared by squeeze casting, Mater. Sci. Eng., A 817 (2021), 141393.
[13] A. Shabani, M.R. Toroghinejad, Study on texture evolution and shear behavior of an Al/Ni/Cu composite, J. Mater. Eng. Perform. (2018) 1–12.
[14] A. Bagheri, M.R. Toroghinejad, A. Taherizadeh, M. Mahmoudi, A. Shabani, Investigation of mechanical properties and corrosion behavior of three-layered brass/interstitial free steel/brass composite manufactured through cold roll bonding process, J. Mater. Eng. Perform. (2022) 1–15.
[15] G.S. Alsoruji, A.M. Sadoun, M. Elmahdy, Microstructure-based modeling and mechanical characteristics of accumulative roll bonded Al nanocomposites with SiC nanoparticles, Metals 12 (11) (2022) 1888.
[16] A. Bagheri, M.R. Toroghinejad, A. Taherizadeh, Effect of roughness and surface hardening on the mechanical properties of three-layered brass/IF steel/brass composite, Trans. Indian Inst. Met. 71 (9) (2018) 2199–2210.
[17] M. Tayyebi, D. Rahmatabadi, A. Karimi, M. Adhami, R. Hashemi, Investigation of annealing treatment on the interfacial and mechanical properties of Al5052/Cu multilayered composites subjected to ARB process, J. Alloys Compd. 871 (2021), 159513.
[18] H. Jafarian, M. Mahdavian, S. Shams, A. Eivani, Microstructure analysis and observation of peculiar mechanical properties of Al/Cu/Zn/Ni multi-layered composite produced by Accumulative-Roll-Bonding (ARB), Mater. Sci. Eng., A 805 (2021), 140556.
[19] S. Jiang, R.L. Peng, Z. Hegedűs, T. Gnäupel-Herold, J. Moverare, U. Lienert, F. Fang, X. Zhao, L. Zuo, N. Jia, Micromechanical behavior of multilayered Ti/Nb composites processed by accumulative roll bonding: an in-situ synchrotron X-ray diffraction investigation, Acta Mater. 205 (2021), 116546.
[20] A. Shabani, M.R. Toroghinejad, A. Shafyei, Fabrication of Al/Ni/Cu composite by accumulative roll bonding and electroplating processes and investigation of its microstructure and mechanical properties, Mater. Sci. Eng., A 558 (2012) 386–393.
[21] W.S. Barakat, M.K. Younis, A. Sadoun, A. Fathy, M.I. Habba, Optimization of the accumulative roll bonding process parameters and SiC content for optimum enhancement in mechanical properties of Al-Ni-SiC composites, Alex. Eng. J. 76 (2023) 131–151.
[22] Y. Saito, H. Utsunomiya, N. Tsuji, T. Sakai, Novel ultra-high straining process for bulk materials—development of the accumulative roll-bonding (ARB) process, Acta Mater. 47 (2) (1999) 579–583.
[23] S.S. Ebrahimi, K. Dehghani, J. Aghazadeh, M. Ghasemian, S. Zangeneh, Investigation on microstructure and mechanical properties of Al/Al-Zn-Mg–Cu laminated composite fabricated by accumulative roll bonding (ARB) process, Mater. Sci. Eng., A 718 (2018) 311–320.
[24] Y. Wang, F. Zhong, R. Wu, H. Wu, N. Turakhodjaev, B. Kudratkhon, J. Sun, L. Hou, J. Zhang, X. Li, High-strength, ductility and modulus Al–Li/B4C composite with near nanostructure produced by accumulative roll bonding, J. Alloys Compd. 834 (2020), 155105.
[25] S. Jiang, R.L. Peng, N. Jia, X. Zhao, L. Zuo, Microstructural and textural evolutions in multilayered Ti/Cu composites processed by accumulative roll bonding, J. Mater. Sci. Technol. 35 (6) (2019) 1165–1174.
[26] M. Raei, M.R. Toroghinejad, R. Jamaati, J.A. Szpunar, Effect of ARB process on textural evolution of AA1100 aluminum alloy, Mater. Sci. Eng., A 527 (26) (2010) 7068–7073.
[27] R. Jamaati, M.R. Toroghinejad, Effect of stacking fault energy on deformation texture development of nanostructured materials produced by the ARB process, Mater. Sci. Eng., A 598 (2014) 263–276.
[28] A. Fattah-Alhosseini, O. Imantalab, Y. Mazaheri, M. Keshavarz, Microstructural evolution, mechanical properties, and strain hardening behavior of ultrafine grained commercial pure copper during the accumulative roll bonding process, Mater. Sci. Eng., A 650 (2016) 8–14.
[29] J. Moradgholi, A. Monshi, K. Farmanesh, M.R. Toroghinejad, M.R. Loghman-Estarki, Comparison of microstructure, toughness, mechanical properties and work hardening of titanium/TiO2 and titanium/SiC composites manufactured by accumulative roll bonding (ARB) process, Ceram. Int. 43 (10) (2017) 7701–7709.
[30] S. Gashti, A. Fattah-Alhosseini, Y. Mazaheri, M. Keshavarz, Effects of grain size and dislocation density on strain hardening behavior of ultrafine grained AA1050 processed by accumulative roll bonding, J. Alloys Compd. 658 (2016) 854–861.
[31] A. Shabani, M.R. Toroghinejad, Investigation of the microstructure and the mechanical properties of Cu-NiC composite produced by accumulative roll bonding and coating processes, J. Mater. Eng. Perform. 24 (12) (2015) 4746–4754.
[32] L. Lutterotti, MAUD, Material Analysis Using Diffraction, 1997, p. 2008. Copyright (c).
[33] A. Chanda, M. De, X-ray characterization of the microstructure of α-CuTi alloys by Rietveld's method, J. Alloys Compd. 313 (1) (2000) 104–114.
[34] A. Shabani, M.R. Toroghinejad, Investigation of microstructure, texture, and mechanical properties of FeCrCuMnNi multiphase high entropy alloy during recrystallization, Mater. Char. 154 (2019) 253–263.
[35] A. Shabani, M.R. Toroghinejad, M. Aminaei, Effect of prior cold deformation on recrystallization behavior of a multi-phase FeCrCuMnNi high entropy alloy, Mater. Chem. Phys. 272 (2021), 124991.
[36] H. Taheri Barayjani, M.R. Toroghinejad, A. Rezaeian, A. Shabani, P. Bocher, An investigation on microstructure and mechanical properties of a copper strip

subjected to different routes of accumulative roll bonding process, J. Mater. Eng. Perform. 32 (2) (2023) 651–659.
[37] J.H. Hollomon, Tensile deformation, Aime Trans 12 (4) (1945) 1–22.
[38] A. Shabani, M.R. Toroghinejad, A. Shafyei, R.E. Logé, Microstructure and mechanical properties of a multiphase FeCrCuMnNi high-entropy alloy, J. Mater. Eng. Perform. 28 (4) (2019) 2388–2398.
[39] N. Afrin, D. Chen, X. Cao, M. Jahazi, Strain hardening behavior of a friction stir welded magnesium alloy, Scripta Mater. 57 (11) (2007) 1004–1007.
[40] A. Shabani, M.R. Toroghinejad, A. Shafyei, R.E. Logé, Evaluation of the mechanical properties of the heat treated FeCrCuMnNi high entropy alloy, Mater. Chem. Phys. 221 (2019) 68–77.
[41] D. Rahmatabadi, M. Tayyebi, A. Sheikhi, R. Hashemi, Fracture toughness investigation of Al1050/Cu/MgAZ31ZB multi-layered composite produced by accumulative roll bonding process, Mater. Sci. Eng., A 734 (2018) 427–436.
[42] M. Alizadeh, M.H. Paydar, High-strength nanostructured Al/B4C composite processed by cross-roll accumulative roll bonding, Mater. Sci. Eng., A 538 (2012) 14–19.
[43] M. Böhme, M.F.-X. Wagner, On the correlation of shear band formation and texture evolution in α-brass during accumulative roll bonding, Scripta Mater. 154 (2018) 172–175.
[44] L. Song, Z. Xie, H. Gao, C. Kong, H. Yu, Microstructure and mechanical properties of ARB-processed AA1050/AA5052 multilayer laminate sheets during cryorolling, Mater. Lett. 307 (2022), 130998.
[45] F.J. Humphreys, M. Hatherly, Recrystallization and Related Annealing Phenomena, Elsevier, 2012.
[46] S. Scudino, Mechanism of shear banding during cold rolling of a bulk metallic glass, J. Alloys Compd. 773 (2019) 883–889.
[47] A. Shabani, M.R. Toroghinejad, A. Shafyei, P. Cavaliere, Effect of Cold-Rolling on Microstructure, Texture and Mechanical Properties of an Equiatomic FeCrCuMnNi High Entropy Alloy, Materialia, 2018.
[48] R. Jamaati, M.R. Toroghinejad, M. Mohtadi-Bonab, H. Edris, J.A. Szpunar, M. R. Salmani, Texture development of ARB-processed steel-based nanocomposite, J. Mater. Eng. Perform. 23 (12) (2014) 4436–4445.
[49] G.S. Alsoruji, A. Sadoun, M. Abd Elaziz, M.A. Al-Betar, A. Abdallah, A. Fathy, On the prediction of the mechanical properties of ultrafine grain Al-TiO2 nanocomposites using a modified long-short term memory model with beluga whale optimizer, J. Mater. Res. Technol. 23 (2023) 4075–4088.
[50] I. Najjar, A. Sadoun, A. Fathy, On the understanding and prediction of tribological properties of Al-TiO2 nanocomposites using artificial neural network, J. Compos. Mater. 57 (14) (2023) 2325–2337.
[51] M.I. Habba, M.K. Younis, A. Sadoun, A. Fathy, W.S. Barakat, On the microstructural and mechanical responses of dual-matrix Al-Ni/SiC composites manufactured using accumulative roll bonding, Alex. Eng. J. 78 (2023) 1–14.
[52] I. Najjar, A. Sadoun, M. Abd Elaziz, H. Ahmadian, A. Fathy, A. Kabeel, Prediction of the tensile properties of ultrafine grained Al–SiC nanocomposites using machine learning, J. Mater. Res. Technol. 24 (2023) 7666–7682.
[53] M. Reihanian, S. Fayezipour, S.M. Lari Baghal, Nanostructured Al/SiC-graphite composites produced by accumulative roll bonding: role of graphite on microstructure, wear and tensile behavior, J. Mater. Eng. Perform. 26 (4) (2017) 1908–1919.
[54] B. Sadeghi, A. Shabani, P. Cavaliere, Hot rolling of spark-plasma-sintered pure aluminium, Powder Metall. 61 (4) (2018) 285–292.